RESEARCH ARTICLE

Flowfield measurements in the wake of a robotic lamprey

**Marcus Hultmark · Megan Leftwich ·
Alexander J. Smits**

Abstract Experiments are reported on the hydrodynamics of a swimming robotic lamprey under conditions of steady swimming and where the thrust exceeds the drag. The motion of the robot was based on the swimming of live lampreys, which is described by an equation similar to that developed for the American eel by Tytell and Lauder (J Exp Biol 207:1825–1841, 2004). For steady swimming, the wake structure closely resembles that of the American eel, where two pairs of same sign vortices are shed each tail beat cycle, giving the wake a 2P structure. Force estimates suggest that the major part of the thrust is produced at or close to the end of the tail.

1 Introduction

Eels, snakes and lampreys are anguilliform swimmers, in that a large part of the body undulates during locomotion. In contrast to carangiform swimmers, such as trout and mackerel, where only the caudal part of the body generates thrust, the flowfield dynamics of anguilliform swimmers is not well understood. In particular, it is not clear what parts of the body are engaged in thrust and drag production.

A recent study by Tytell and Lauder (2004) investigated the wake structure developed by a steadily swimming American eel using Particle Imaging Velocimetry (PIV). It was found that for every tail beat two same sign vortices were created. They also found that the most striking feature of the wake is the size and strength of the lateral jets and the notable absence of substantial downstream flow (Tytell and Lauder 2004). This wake structure, with two vortices per tail beat, has also been noted by Müller et al. (2001). A stopping-starting vortex is produced each time the tail reaches a lateral maximum and changes direction. As to the secondary vortex, Müller et al. (2001) suggested that it was created as a result of a phase difference between the body and the tail. In contrast, Tytell and Lauder suggested that when the tail starts to move after changing direction, a low pressure region is created that sucks fluid laterally. When this fluid is shed from the tail it stretches the first vortex and creates a new, same-sign, vortex.

Tytell (2004) found that the American eel swims steadily at a Strouhal number of 0.32 and that the Strouhal number increased slightly when the eel was swimming at lower speeds. The Strouhal number St is a non-dimensional frequency defined by

$$St = \frac{Af}{U}, \tag{1}$$

where f is the frequency of the tail oscillation, A is its peak-to-peak amplitude, and U is the swimming speed.

Triantafyllou et al. (1993) investigated the optimal frequency of a two-dimensional pitching airfoil using linear stability analysis on the mean wake profile, under conditions of maximum efficiency. They argued that the frequency of optimal efficiency is found at the frequency of maximum amplification. They found that the Strouhal number for maximum efficiency was between 0.25 and 0.35 with a most likely value of 0.30. Strouhal number for the most fish in steady swimming have also been reported

M. Hultmark · M. Leftwich · A. J. Smits (✉)
Mechanical and Aerospace Engineering, Princeton University,
Princeton, NJ 08540, USA
e-mail: asmits@princeton.edu

Present Address:
M. Hultmark
Chalmers University of Technology, 41296 Gothenburg, Sweden

to be close to the predicted value for optimal efficiency (Triantafyllou et al. 1993).

A recent study by Buchholz and Smits (2007) investigated the flow field in the wake of a pitching flat plate, taken as a simplified tail of a fish without heave. Buchholz and Smits found that the wake consisted of three-dimensional vortex loops linked together in a complicated vortex chain (see Fig. 1). It was found that the width of the wake increased with increasing St, and that two modes of wake structure exist. For lower Strouhal numbers a single vortex is shed each half cycle, and a vortex of opposite sign is shed in the next half cycle. This structure was found for Strouhal numbers between 0.2 and 0.25, and it is shown in Fig. 1. Following Williamson and Roshko (1998), this is described as a 2S structure because two single vortices are shed each cycle. As the Strouhal number increases, the wake broadens and two vortices of opposite sign are shed each half cycle, that is, it resembles a 2P structure (Buchholz and Smits 2007).

Kern and Koumoutsakos (2006) investigated the thrust production of an anguilliform swimmer by numerical simulation and found that the anterior half of the body had no contribution to the thrust. While the majority of the thrust was produced at the tail, there was also some thrust produced by the posterior part of the body. Lighthill's inviscid elongated body theory (Lighthill 1971) predicts the efficiency of a carangiform swimmer to be much higher than the efficiency of an anguilliform swimmer, but this model assumes that thrust is produced only at the trailing edge (that is, right at the tail).

Here, we are interested in the hydrodynamics of lamprey locomotion. Lampreys (*Ichthyomyzon unicuspis*) are jawless fish (see Fig. 2) that resemble eels in their swimming motion. Lampreys are one of the simplest vertebrates and their behavior may give insight on the locomotion of higher vertebrates. As the lamprey swims, we see a complex behavior that involves rhythmic output from each spinal segment or functional group of motoneurons. This output derives from the central pattern generator (CPG) neural circuitry that periodically activates muscles and muscle
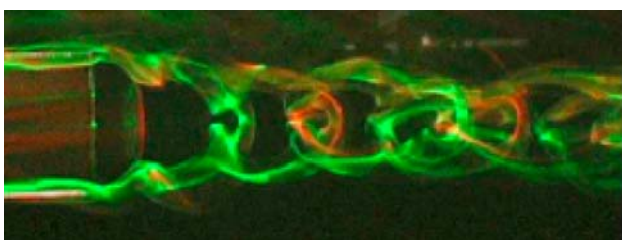

Fig. 1 Flow visualization of the wake produced by a flapping rectangular plate at a Strouhal number of 0.23. Flow is from *left* to *right*. The *red* and *green* dyes originate on opposite sides of the plate. From Buchholz and Smits (2007)

Fig. 2 The silver lamprey, *Ichthyomyzon unicuspis*, © Clifford Kraft

groups. Periodic CPG bursting must be coordinated to maintain the proper phase relationships among the muscles, a task performed by the intersegmental coordinating system. The muscles must then move the limbs and/or body parts through the water. The resulting motions cause mechanical reaction forces on the body, depending upon task and environment, and body movements in turn generate sensory feedback signals to the CPG that can reshape and retime the rhythm or its components to produce appropriate muscle forces and velocities. In terms of the body hydrodynamics, we aim to understand the wake structure, the forces acting on the body, and the possible feedback between the CPG and the hydrodynamics, specifically through neuromast organs located on the exterior of the body.

Because of the difficulties involved in working with live lampreys, a robotic lamprey is used to study the flowfield. The kinematics of the body motion are based on the study of live animals. PIV is used to examine the flowfield over the body and the structures in the wake in steady swimming, and where the thrust exceeds the drag. By integrating the flowfield, estimates of the resultant force are made, which can then be used to investigate the relative contributions made by different parts of the body.

2 Experiment

The swimming motions of live lampreys were studied at the University of Maryland. The animals were filmed while swimming in a small water channel ($110 \times 20 \times 20$ cm) using a DRS Lightning RDT/1 high speed digital video camera with Midas 2.0 (Xcitex, Cambridge, MA, USA) at 60 frames per second. The camera was mounted above the channel and was able to capture up to five tail beats before the fish swam out of view. The film clips of the swimming lamprey were analyzed using a custom Matlab R2006b program that finds the centerline of the lamprey body at every instant.

A recent study by Tytell and Lauder (2004) investigated the kinematics of a steadily swimming American eel and described the motion of the eel centerline by an exponentially growing traveling wave. That is,

$$y(s) = Ae^{[\alpha(s/L-1)]} \sin\left[\frac{2\pi}{\lambda}(s - Vt)\right] \tag{2}$$

where y is the lateral position of the midline, s is the coordinate following the midline, A is the tail beat

Table 1 Parameters for Eq. 2

	Amplitude, A	Growth rate, α	Body wavelength, λ	Wave speed, V
Lamprey	0.089	2.18	0.642	1.404
Eel	0.069	2.76	0.604	1.878

The eel parameters are taken from Tytell and Lauder (2004)

amplitude, α is the amplitude growth rate, L is the body length, λ is the wave length, t is time and V is the wave speed. It was found here that Eq. 2 also describes lamprey motion accurately, and therefore Eq. 2 was fitted to the points of the centerline with a correction for a possible angle of the lamprey relative to the camera. The lampreys moved at a steady swimming speed between 0.5 and 1.5 L/s. The parameters are given in Table 1 where a comparison with Tytell and Lauder's (2004) results on the American eel are also given.

The kinematics of the live animal swimming was used to generate the motion of the robotic lamprey. The robot consists of 13 Hitech HS-945MG Coreless Ultra Torque servomotors (see Fig. 3) connected together by rigid links. Each servomotor is controlled through a BasicX microcontroller mounted in the "head" of the robotic lamprey. A custom Matlab program converts the coordinates given by Eq. 2 to coordinates based on the angle at each point. This is uploaded by BasicX to the microprocessor. When a given servomotor is actuated, the shaft of the servomotor will move to the specific angular position and hold that position as long as the actuation is unchanged. In this way a traveling wave is generated along the robot body at the desired wave speed.

The robot is powered by 12 rechargeable 2,500 mAh AA batteries, each 1.2 V, connected in two groups of six batteries connected in series to give an output voltage of 7.2 V for the servomotors.

A foam skeleton was wrapped around the servomotors to create a more realistic cross-section and a smoother exterior. A waterproof skin covered the foam skeleton. The skin was made of Cementex vulcanizeable natural Latex with low ammonium content (#80 VLA). A model form was painted with three to five layers of liquid latex. Each layer was allowed to dry before applying the next layer. The skin was then vulcanized for 20 h at room temperature. The skin of the robotic lamprey captures the general

Fig. 3 The image shows the 13 servomotors comprising the robotic lamprey. Each servomotor is connected to its neighbours by rigid links

form of the animal without anal or dorsal fins. The foam skeleton trapped air inside the robot to help make it neutrally buoyant. Weights were added inside the tail of the robot to make fine adjustments on balance and buoyancy. The total length of the robot was $L = 1.14$ m, with a typical cross-section measuring 38 mm $\times$ 97 mm.

The flow over the body of the robot and in the wake were investigated using PIV in a plane containing the body motion. The experiments were conducted in a closed loop, free surface water channel with a test section that is 0.46 m wide, 0.3 m deep, and 2.5 m long (see Fig. 4). Upstream of the 5:1 contraction is one honeycomb and three screens. The front part of the robot was held in the test section at mid-depth by a frame mounted on an air-bearing sled free to move in the streamwise direction. The steady swimming condition was set by matching the flow speed in the channel to the swimming speed of the robot (neglecting the friction in the air-bearing system). Surface waves were eliminated by mounting a clear acrylic plate so that it was in contact with the free surface.

Silver coated hollow ceramic spheres with a diameter of 100 μm were used as seeding particles (Potters Industries Inc. Conduct-O-Fil AGSL150 TRD). A Spectra Physics 2020 Argon laser was used to create a light sheet using an optical fiber delivery system and a Powell lens (Oz Optics Ltd). The sheet thickness was typically 1.5 mm (1/e thickness). A Redlake MotionXtra HG-LE camera was used to capture the PIV images. The camera has a resolution of 1,128 $\times$ 752 pixels and can capture a total of 1,263 frames at up to 1,000 fps. It is equipped with a Burst Record on Command (BROC) function that allows it to take a specified number of images at every trigger signal with an adjustable frequency. The camera could also be used with an external triggering device and a Stanford Research Systems DG535 Digital Delay/Pulse Generator was used to control the camera timing and generate image pairs with a time delay of 8 ms between images. Exposure times were typically 3 ms.

3 Results

The actual motion of the robotic lamprey is compared with the input according to Eq. 2 in Fig. 5. The motion of the robot surface is filtered by the presence of the foam skeleton and the flexible, waterproof skin, but it is clear that the largest discrepancies occur near the tail. To minimize this discrepancy, the length of the last rigid segment was minimized and a short, flexible section was added to the tail.

Figure 6 shows the instantaneous velocity fields in the wake of the robotic lamprey under conditions where thrust and drag are matched so that the robot is swimming

Fig. 4 Sketch of the water channel showing the laser sheet and camera arrangements. **a** *Top* view and **b** *side* view
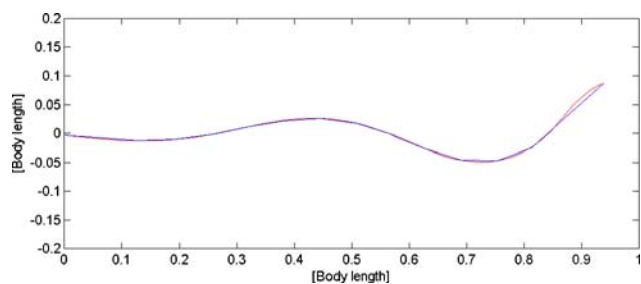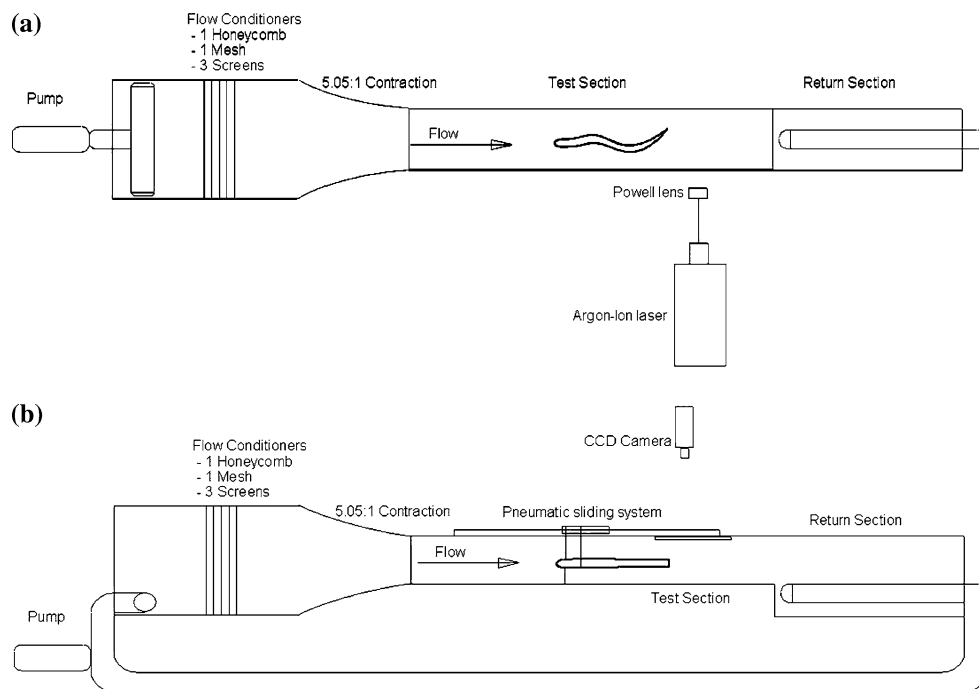

Fig. 5 Comparison between lamprey (*red line*) and robot waveforms (*blue line*). The robotic lamprey motion is the approximation due to 13 connected segments

steadily (flow speed of 9.5 cm/s, and $St = 0.65$). The Strouhal number at which the robotic lamprey swims steadily is between 0.6 and 0.65. This can be compared with a living lamprey which typically swims steadily at a Strouhal between 0.3 and 0.35. The discrepancy is probably due to the higher drag associated with the robot, so that the robot tail beat frequency needs to be higher to develop a larger thrust required to balance the increased drag. It is noted that the Reynolds number of the robot based on length of the robotic lamprey is approximately 1.15×10^5 where the live animal typically has a Reynolds number around 6×10^4. No attempt was made to match Reynolds number. Figure 7 shows the wake at the same conditions but the flow fields are phase-averaged over 35 periods. The phase averaged velocity fields contain less noise than the instantaneous ones but the principal features are the same,
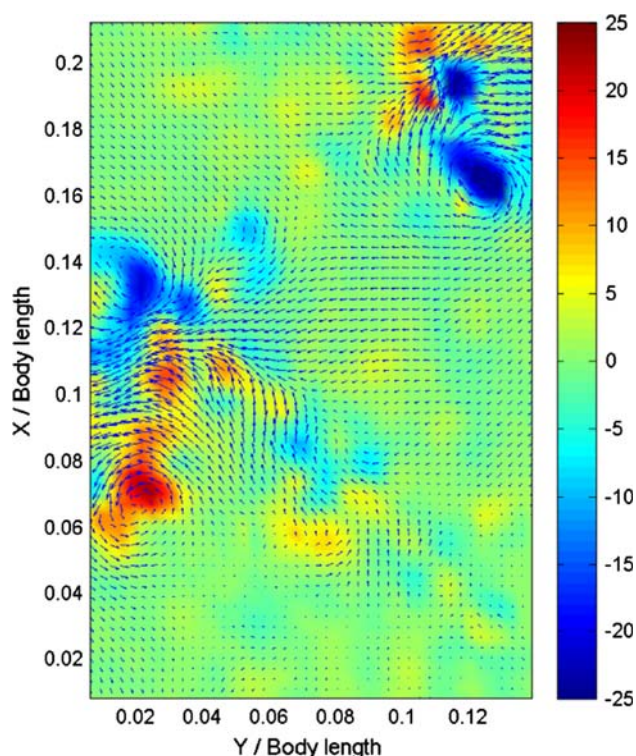

Fig. 6 Example of instantaneous velocity and vorticity fields in the wake of the steady swimming robot. The vectors represent the velocity field with the convective velocity subtracted, and the *background color* represents the out-of-plane vorticity. The flow is from *top* to *bottom*, and the tail of the robot is just out of the picture at the *top*

Fig. 7 Phase-averaged velocity and vorticity fields in the wake of the steady swimming robot. The vectors represent the velocity field with the convective velocity subtracted, and the *background color* represents the out-of-plane vorticity. The flow is from *top* to *bottom*, and the tail of the robot is indicated by the *small black wedge* near the *top* of each image
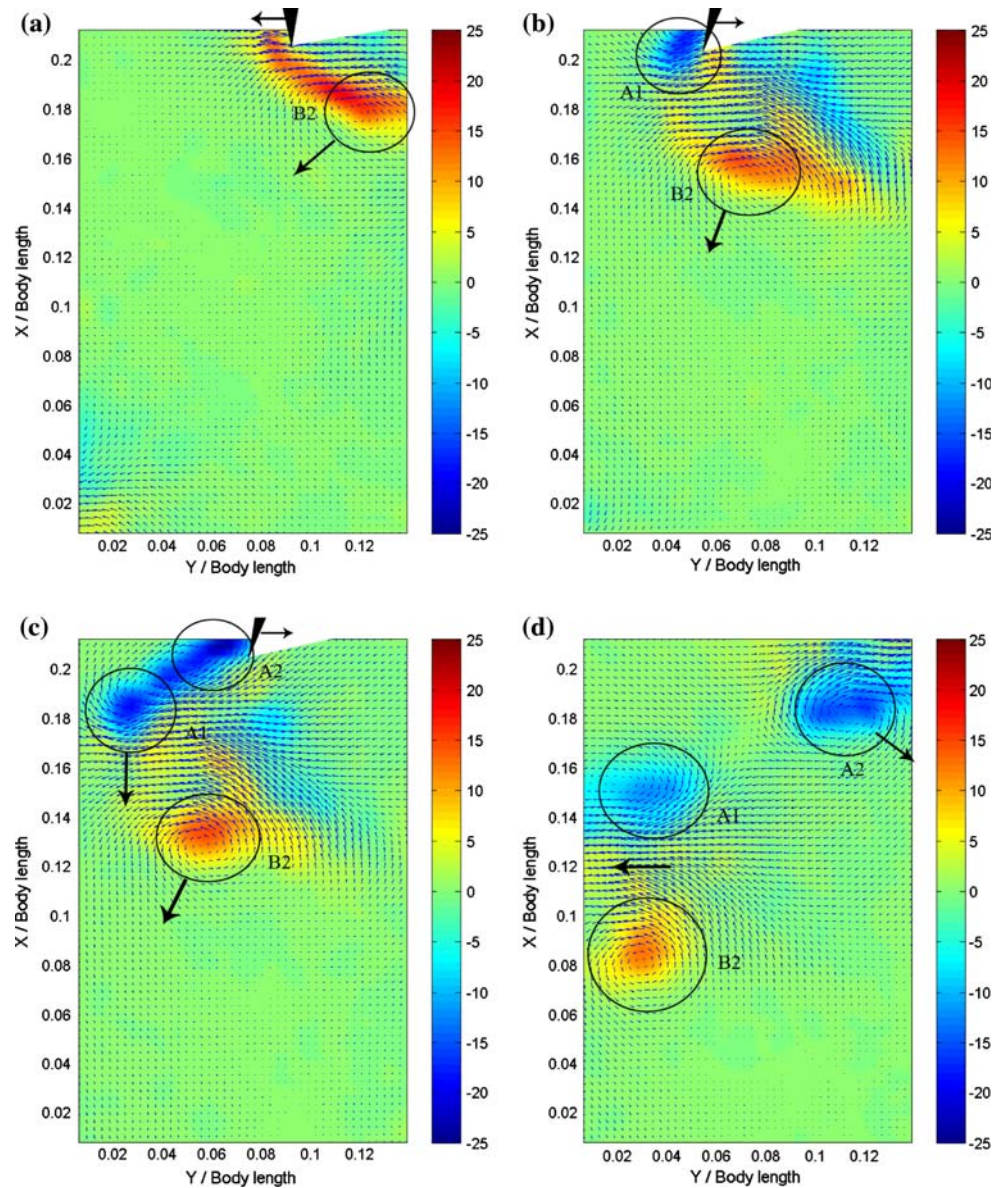

indicating that the motion of the robotic lamprey is highly repetitive.

The data show that two same sign vortices are created at every tail beat. In Fig. 7a the tail is moving to the left, transporting positive vorticity from the last tail beat. In Fig. 7b the tail has just passed its extrema and is moving to the right. A stopping-starting vortex is created with negative vorticity (A1, the primary vortex), and the vorticity that was transported from the other side of the wake has separated from the tail and is moving downstream and to the left. A "jet" marked by an arrow, is induced between the two vortices. When the tail has moved further to the right (Fig. 7c), the primary vortex is stretched out and a secondary vortex can be distinguished (A2). The vortex seen in Fig. 7a is the secondary vortex from the last tail beat (B2). The primary vortex (A1) is completely separate

from the secondary vortex (A2) and shed directly in the wake (see Fig. 7d). At a steady swimming speed, the primary and the secondary vortex from the tail beat 180° earlier (A1 and B2) align in the streamwise direction so that they induce a jet between them normal to the direction of forward motion (see Fig. 7d). In the same figure it can be seen that the secondary vortex (A2) is transported by the tail to the other side of the wake where it will have the same role as B2 had earlier.

The flowfield generated by the robot may be compared to the results obtained by Tytell and Lauder (2004) (see Fig. 8a). The similarities in the structure of the two wakes are striking. The two counter-rotating vortices and the induced lateral jet are apparent in both wakes, and the magnitude and distribution of the vorticity is very similar, including the trail of vorticity from the tail to the primary

Fig. 8 Phase averaged velocity fields in the wake of **a** an American eel, taken from Tytell and Lauder (2004). **b** The robotic lamprey. Both represent the field at the same phase of motion
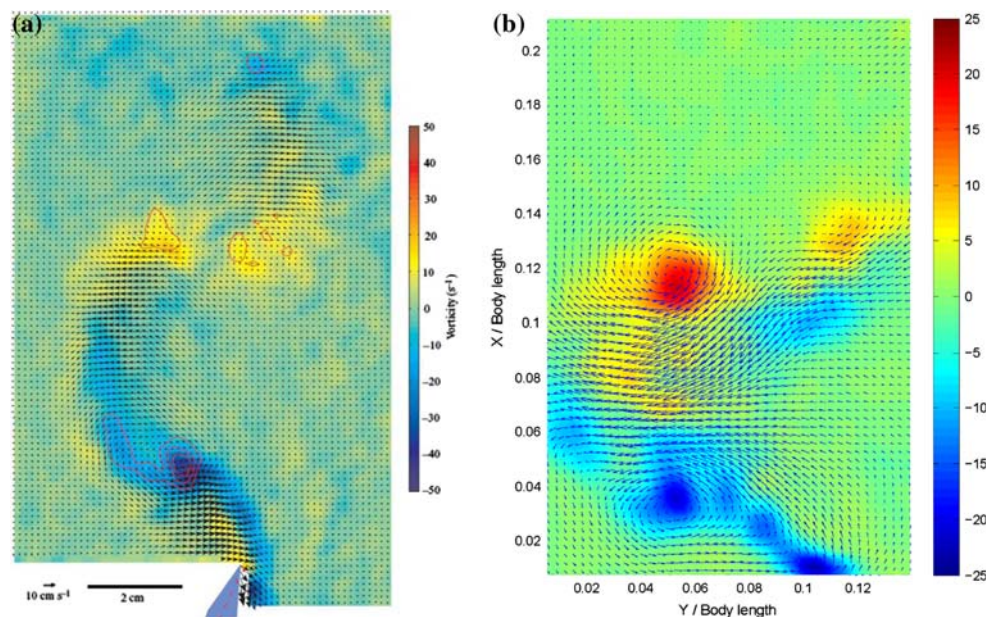
vortex and the area of positive vorticity on the right hand side. However, the wake of the robotic lamprey spreads more quickly, primarily because the robot is operating at a higher Strouhal number than the eel (0.65 compared to 0.32).

For cases where the thrust is greater than the drag, the jet induced between the primary and secondary vortices will have a component in the streamwise direction. Figure 9 shows the wake of the robotic lamprey when the thrust exceeds the drag, with the arrow indicating the direction of the induced jet (flow speed of 9.5 cm/s, and $St = 0.65$). To estimate the direction of the resultant force on the robot as a function of Strouhal number, the momentum flux, $\rho \vec{U}(\vec{n} \cdot \vec{U})$, was integrated over a control volume bounded by the half wake (see Fig. 6) for each image. The integration was done in the symmetry plane corresponding at the middle of the robot, and all out-of plane motions were neglected. The results were summed for an entire cycle to find the time-averaged force direction. The Strouhal number was varied by changing the free stream velocity at a constant tail beat frequency $f = 0.56$ Hz and amplitude $A = 15$ cm. The results are shown in Fig. 10. The angle is defined positive downstream so that the net momentum flux in the downstream direction increases as the Strouhal number increases (flow speed decreasing). For a freestream velocity of 9.5 cm/s (corresponding to the results given in Figs. 6, 7), the resulting angle is 0.38°, confirming that this condition closely approximates the condition of steady swimming. At higher Strouhal numbers, where the thrust exceeds the drag, the wake is wider than in steady swimming because the convection velocity of the vortices is lower while their induced velocity is not reduced as much. This is the same behavior Buchholz and Smits (2007)
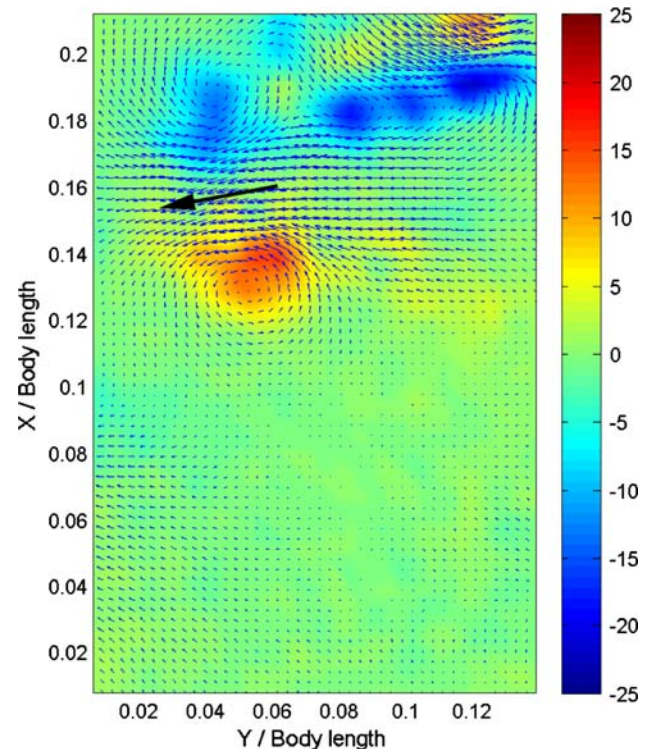

Fig. 9 An example of the phase-averaged velocity and vorticity fields in the wake of the robot when the thrust exceeds the drag

found in the wake of a flat plat at increased Strouhal number.

Figure 11 shows the instantaneous velocity and vorticity fields along the body of the robot. A relatively low level of vorticity are seen in the region near the body, and it seems to be confined to the boundary layer rather than being shed and convected downstream, so that it is unlikely to
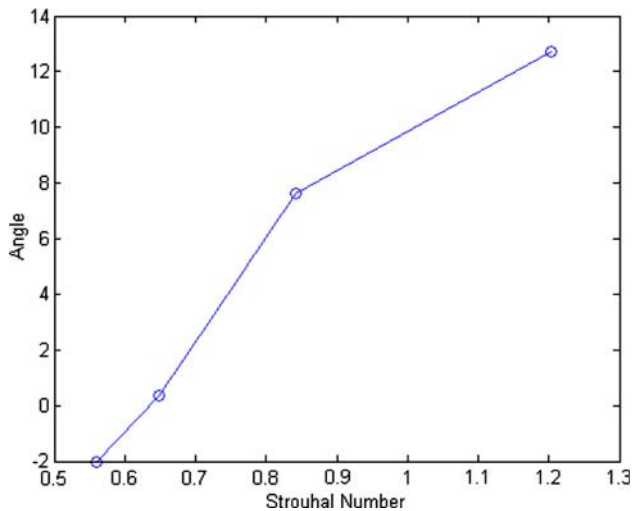
Fig. 10 Angle of force vector plotted against the Strouhal number. *Positive values* indicate that the resultant force acts to accelerate the robot

contribute significantly to the thrust. The side-to-side motion of the robot generates alternating favorable and unfavorable pressure gradients along the body, and this causes the vortical region to expand as the robot moves to the right in Fig. 11b. When the tail changes directions, the pressure gradients change signs and the region of vorticity becomes thinner, as seen in Fig. 11c.

To further determine if thrust is produced in this region, the momentum flux may be integrated over the boundaries of a two-dimensional control volume containing the wake and parts of the tail. By varying the size of the box to include progressively more of the body, the net force acting on particular parts of the body may be identified (subject to the restrictions on the analysis, particularly the assumption of two-dimensionality). Figure 12 shows the results using two different starting points for the control volume. Where the two volumes overlap it is clear that the forces in this region match. The tip of the tail is at $x/L = 0$, where x is positive upstream. Because this method estimates the total force produced by the sections downstream, it is the slope of the curve that indicates the resultant force production at a specific point rather than the absolute value. The slope is steep around $x/L = 0$ which suggests that this part of the body is responsible for the majority of the force production. Between $x/L = 0.01$ and $x/L = 0.1$ the force is approximately constant, suggesting that the thrust produced in this region is balanced by the local drag contribution. At x-locations upstream of $x/L = 0.1$ the slope is negative which implies that the drag produced is greater than the thrust.

4 Conclusions

Particle image velocimetry was employed to obtain the instantaneous flowfield in the wake behind a robotic lamprey while swimming in a water channel, as well as over the body of the robot. Two same-sign vortices are produced for every tail beat and a jet is induced between the primary vortex produced from one tail beat and the secondary vortex produced from the previous tail beat. This jet is normal to the direction of forward motion while the robot is

Fig. 11 Phase-averaged velocity and vorticity fields along the body and in the wake for a steadily swimming robot. The *vectors* represent the velocity field with the convective velocity subtracted, and the *background color* represents the out-of-plane vorticity. The flow is from *top* to *bottom*, and the body of the robot is indicated by the *black shape*
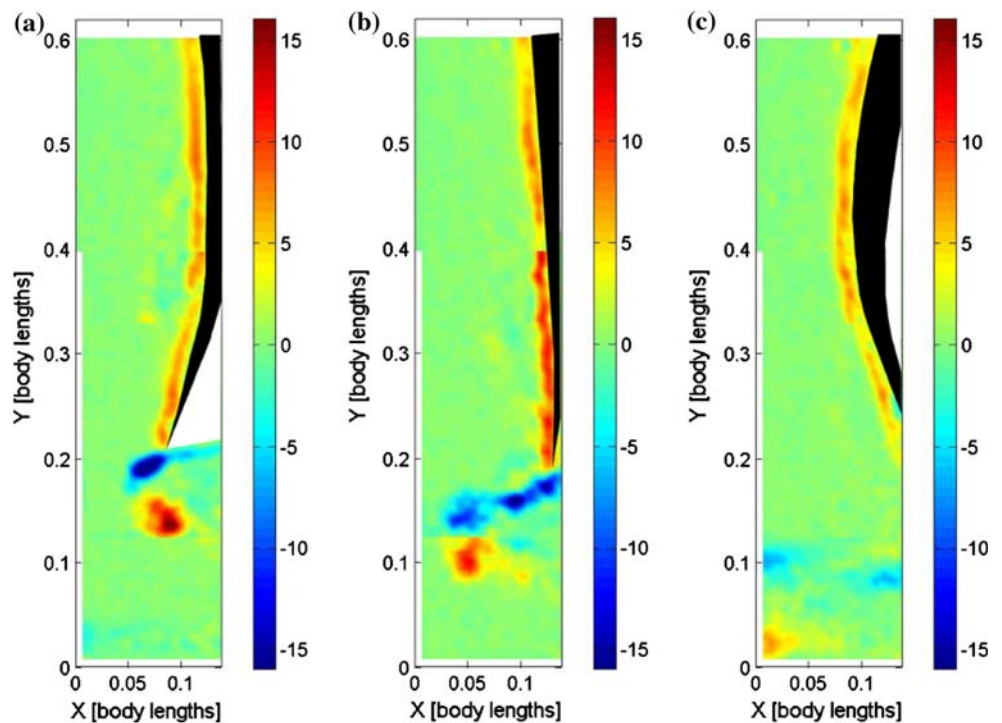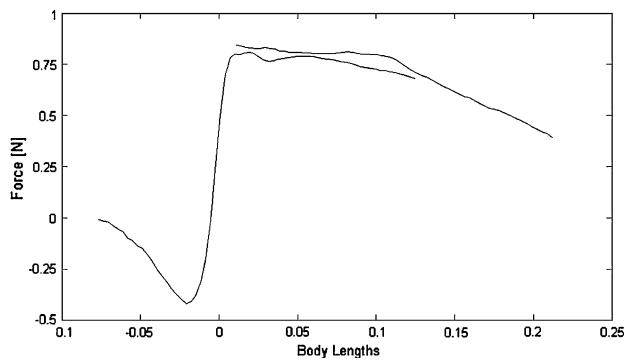
Fig. 12 The force produced from the wake to different *x/L* locations along the body (*x/L* = 0 is the tip of the tail). The *blue curve* is derived using one control volume only, and the *red curve* is derived from combining two control volumes to extend the domain

swimming steadily. When the thrust exceeds the drag the induced jet has a streamwise component.

The wake of the robotic lamprey appears to be similar to the wake produced by anguilliform fish. In particular, the 2P wake structure produced at steady swimming is very similar to that observed for the American eel by Tytell and Lauder (2004).

The velocity and vorticity fields along the body suggest that net thrust production occurs primarily at, or close to, the tail. This conclusion was supported by estimates of the resultant force using a control volume approach, which indicated that although some thrust is produced by the

posterior part of the body, it is almost balanced by the local drag contribution.

References

Buchholz JH, Smits AJ (2007) On the evolution of the wake structure produced by a low aspect ration pitching panel. J Fluid Mech 546:433–443

Kern S, Koumoutsakos P (2006) Simulations of optimized anguilliform swimming. J Exp Biol 209:4841–4857

Lighthill MJ (1971) Large-amplitude elongated-body theory of fish locomotion. Proc R Soc Lond B 179:125–138

Müller UK, Smit J, Stamhuis EJ, Videler JJ (2001) How the body contributes to the wake in undulatory fish swimming: flow fields of a swimming eel (anguilla anguilla). J Exp Biol 204:2751–2762

Triantafyllou GS, Triantafyllou MS, Grosenbaugh MA (1993) Optimal thrust development in oscillating foils with application to fish propulsion. J Exp Biol 7:205–224

Tytell ED (2004) The hydrodynamics and eel swimming ii: effects of swimming speed. J Exp Biol 207:3265–3279

Tytell ED, Lauder GV (2004) The hydrodynamics and eel swimming 1: wake structure. J Exp Biol 207:1825–1841

Williamson CHK, Roshkol A (1998) The hydrodynamics and eel swimming ii: effects of swimming speedvortex formation in the wake of an oscillating cylinder. J Fluid Struct 2:355–381